ENGINEERING

Optimal sparsity allows reliable system-aware restoration of fluorescence microscopy images

Biagio Mandracchia[1,2,3]*, Wenhao Liu[1], Xuanwen Hua[1], Parvin Forghani[4], Soojung Lee[1], Jessica Hou[5], Shuyi Nie[5,6], Chunhui Xu[4,6], Shu Jia[1,6]*

Fluorescence microscopy is one of the most indispensable and informative driving forces for biological research, but the extent of observable biological phenomena is essentially determined by the content and quality of the acquired images. To address the different noise sources that can degrade these images, we introduce an algorithm for multiscale image restoration through optimally sparse representation (MIRO). MIRO is a deterministic framework that models the acquisition process and uses pixelwise noise correction to improve image quality. Our study demonstrates that this approach yields a remarkable restoration of the fluorescence signal for a wide range of microscopy systems, regardless of the detector used (e.g., electron-multiplying charge-coupled device, scientific complementary metal-oxide semiconductor, or photomultiplier tube). MIRO improves current imaging capabilities, enabling fast, low-light optical microscopy, accurate image analysis, and robust machine intelligence when integrated with deep neural networks. This expands the range of biological knowledge that can be obtained from fluorescence microscopy.

INTRODUCTION

Faithful recording and displaying of diverse anatomical and functional signals within the densely packed cellular space unfold the basic details of living organisms. In this regard, fluorescence microscopy has been a revolutionary driving force for biological research. In essence, all fluorescence microscopes can allocate a finite photon budget from biological specimens for interrogation at various spatiotemporal scales. However, the sensitivity of current sensors to the influx of photons remains nonideal and exhibits pixel-to-pixel variation, leading to the uncertainty of photon detection (*1*). The resultant noise inevitably produces artifacts and hinders accurate observation of fluorescent signals, impairing fast, low-light, and quantitative imaging (*2*–*6*).

Physically, the nonideal photon detection results from mixed processes owing to imaging conditions and sensor architecture (*7*). For fluorescence microscopy, these processes can be grouped into four major categories—charge-to-voltage conversion (read noise), photon-detector interaction (photon shot noise), thermal currents (dark shot noise), and pixel nonuniformity (fixed pattern noise) (section S1.1). Various strategies for image restoration have been developed to exploit noise statistics using models such as signal-independent additive white Gaussian noise (*8*–*10*) or spatially variant mixed Poisson-Gaussian noise (*11*–*14*). However, classical denoising methods perform less satisfactorily for fluorescent image processing. This is mainly due to the trade-off between noise correction and detail preservation under low-light conditions and the lack of consideration for the actual microscopy system or relevant noise sources such as dark or fixed-pattern noise (*15*, *16*). Recent years have witnessed the development of denoising models that address fluorescence microscopy (*17*–*20*), but their applicability remains limited to specific microscopy or camera types (e.g., multiphoton microscopy (*17*) or scientific complementary metal-oxide semiconductor (sCMOS) cameras (*18*, *19*)). Therefore, a deterministic, generalizable solution for effective image restoration throughout major microscope systems remains unexplored yet highly demanded.

Here, we introduce MIRO, an algorithm for multiscale image restoration based on the optimally sparse representation of fluorescence microscopy data. MIRO formulates an adaptive framework that encompasses camera modeling, pixelwise noise correction, and sparse filtering to correct all microscopy-relevant noise sources. Contrary to existing approaches, MIRO is based on a theoretical model that considers all common pattern, uniform, and nonuniform noise statistics and leverages shearlet optimal sparse representation to extract biological features from noise. To this end, we devised a microlocal domain shrinkage strategy that efficiently extracts the fluorescence signal at multiple scales, achieving quantitative image restoration with substantially enhanced accuracy. Applying this method, we have demonstrated its usability and significance by showing considerable improvements in a variety of fluorescence microscopy techniques and downstream image analysis. Last, we have synergized MIRO with deep learning to use deterministic a priori knowledge in conjunction with neural networks to simplify and optimize the training task. We anticipate that this hybrid approach could offer a promising pathway to further integrate sparsity and machine intelligence for enhanced denoising quality, speed, and generalizability in imaging discoveries.

[1]Wallace H. Coulter Department of Biomedical Engineering, Georgia Institute of Technology and Emory University, Atlanta, GA, USA. [2]Scientific-Technical Central Units, Instituto de Salud Carlos III (ISCIII), Majadahonda, Spain. [3]ETSI Telecomunicación, Universidad de Valladolid, Valladolid, Spain. [4]Department of Pediatrics, School of Medicine, Emory University, Atlanta, GA, USA. [5]School of Biological Sciences, Georgia Institute of Technology, Atlanta, GA, USA. [6]Parker H. Petit Institute for Bioengineering and Bioscience, Georgia Institute of Technology, Atlanta, GA, USA.
*Corresponding author. Email: biagio.mandracchia@uva.es (B.M.); shu.jia@gatech.edu (S.J.)

RESULTS

MIRO framework: Concept and characterization

Digital sensors are composed of different elements that convert the impinging photons (S) into electrons and electrons into a digital number (DN). Each of these elements introduces uncertainty to the detection process, which theoretically can be modeled as

$$DN(p,t) = g(p) \cdot (\mathcal{P}\{S;p,t\} + P\{I_D\tau;p\} + G\{0,\sigma_R^2;p\} + \mathcal{G}\{0,\sigma_{FPN}^2;p,t\}) + o(p) \quad (1)$$

where $\mathcal{P}\{\cdot\}$ indicates the Poisson distribution, $\mathcal{P}\{\cdot,p\}$ the heteroskedastic Gaussian distribution, I_D the dark current, τ the camera exposure time, $g(p)$ the pixel gain, $o(p)$ the offset, and σ_R^2 and σ_{FPN}^2 the variance of readout and fixed pattern noise, respectively (section S1.2).

The MIRO image restoration comprises three main stages (fig. S1). First, it corrects the pixel output using a calibrated map of the offset, gain, and variance for each pixel. This step removes the uncertainty correlated with the spatial variance of the pixel response across the sensor, σ_{FPN}^2, which results in the nonuniform collection efficiency for each pixel. Then, once pixel response nonuniformity is removed, the remaining noise contribution can be modeled as a heteroskedastic Gaussian distribution, i.e., with a spatially varying noise variance. This has been shown to be a reasonable approximation even at low-photon regimes (S < 10 photons per pixel, see section S1.2.2), so we can write

$$I(p,t) \approx \mathcal{G}\{S, S + I_D\tau + \sigma_R^2; p,t\} + o'(p,t) \quad (2)$$

where $o'(p,\tau) = o(p) + g(p) \cdot I_D(p)\tau$ (section S1.3).

Next, to correct the time-dependent noise component and retrieve the signal S, MIRO uses the optimal sparsity conferred by the shearlet transform (*21*) (section S1.4). Shearlets are an emerging extension of wavelets that allow for multiscale analysis with the efficient encoding of anisotropic features, particularly relevant to biological phenomena (*22*–*24*). Shearlets provide optimally sparse representation for a large class of multivariable, multidimensional functions, allowing for simplified mathematical analysis and fast algorithmic implementation (*25*–*27*). Exploiting the shearlet transform for fluorescence images, we then conducted transform-domain thresholding to restore the input signal. We derived a microlocal analysis to estimate and correct noise for each voxel in the shearlet space, avoiding any assumptions about the noise uniformity (Fig. 1, A to D, and section S1.4). Last, lingering noise can be further reduced by taking advantage of the nonlocal similarity of the imaged sample (section S1.5).

To characterize the performance of MIRO, we used both numerical and experimental datasets of varying signal-to-noise ratios (SNRs), resolution, and sampling rates. Specifically, we simulated fluorescence acquisitions in the presence of all the microscopy-relevant noise sources and restored the images using MIRO under different SNR conditions (Fig. 1, E to L). As observed, MIRO allows for the removal of fixed-pattern, dark, and readout noise and a remarkable reduction of photon shot noise, exhibiting an improvement of ~90% over the ideal camera behavior (i.e., containing pure photon shot noise) even at low photon counts (<3 photons per pixel, Fig. 1M). The experimental data processed under similar conditions showed robust and accurate noise correction in accord with the simulated results (section S2.1). Moreover, we assessed using both numerical and experimental data that MIRO can effectively restore the image quality without feature smoothening. On the contrary, our results showed a substantial resolution recovery even at low SNRs due to the reduction of the detrimental noise influence that deteriorates resolution (section S2.2).

Furthermore, we examined the performance of MIRO at varying sampling rates commonly adopted for fluorescence microscopy. In practice, an optimal sampling rate to balance the SNR and detail preservation may not be achieved because of the actual imaging configuration and the fact that major noise sources exist at all sampling rates. Here, we demonstrated the viability of MIRO to perform consistent noise correction independently from the image sampling rate (section S2.3). The results also confirmed the robustness of MIRO noise correction as the sampling rate affects the image sparsity, especially when below the Nyquist limit. Last, we used quantitative metrics such as peak SNR and structural similarity index (SSIM) to measure image enhancement for sparse and dense samples. In both cases, we observed improved image restoration compared to several state-of-the-art denoising methods (section S2.4).

Sensor-agnostic restoration of fluorescence microscopy images

To show general usability, we first implemented MIRO to process images obtained using a wide range of fluorescence microscopy techniques. As validated, MIRO provides effective noise correction and recovers the image quality and resolution for microscopy systems diversely equipped with sCMOS, electron-multiplying charge-coupled device (EMCCD), and photomultiplier tube (PMT) detectors (Fig. 1, N to V). Notably, the MIRO restoration allows for consistent biological observation at a photon budget two orders of magnitude lower with no noticeable loss of image quality, empowering standard microscopy with better temporal resolution and less photodamage (fig. S2 and table S1).

In addition, effective noise removal can enhance quantitative image analysis and, thereby, the range of biological knowledge that can be extracted from fluorescence microscopy data (*28*, *29*). For instance, the presence of noise can complicate the interrogation of subcellular morphology and dynamic processes. Using MIRO for live-cell imaging, dim subcellular objects observed with conventional epifluorescence microscopy can be distinguished with higher clarity, which leads to the improved identification of subcellular organelles (fig. S3 and movies S1 and S2). Notably, MIRO exhibited viable and consistent noise correction without oversmoothening the dense cellular regions that contain substantial nonuniform shot noise due to the diffuse background (Fig. 2, A to F, and movie S3). Such robustness allows for integrating MIRO with image analysis tools and procedures for better biological interrogation. For example, the use of MIRO before Mitometer (*30*) can effectively suppress the misidentification of mitochondrial objects and their trajectories, resulting in improved automated mitochondrial segmentation and tracking during fast time-lapse observations (Fig. 2, G and H).

Next, we validated MIRO restoration for three-dimensional (3D) microscopy image formation. Laser scanning confocal microscopy (LSCM) is a major imaging technique that offers optical sectioning and 3D imaging capability (*31*, *32*). However, conventional LSCM setups are typically equipped with single-pixel PMT detectors with a low quantum efficiency (<30%). This deficiency is usually addressed by increasing the laser power or scan duration (pixel dwell time ≥ 1

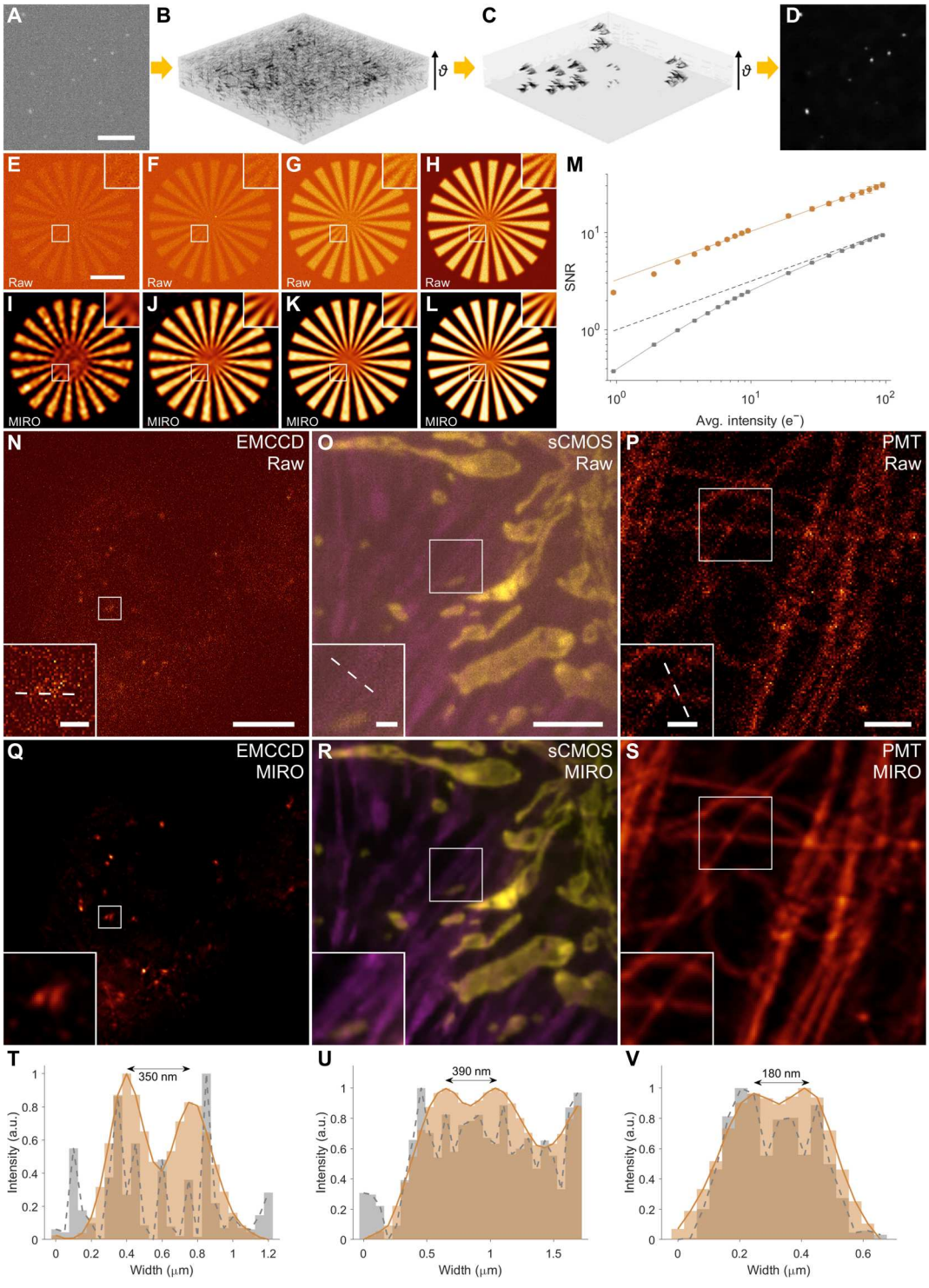

Fig. 1. Multiscale processing through optimal sparsity enables system-aware image restoration. (**A** to **D**) Concept of microlocal shearlet shrinkage for MIRO image restoration. The input fluorescent image (A) is transformed to the shearlet space (B), where the spatially overlapping noise and signal features become microlocally distinguishable across shearlet components (ϑ). MIRO pipeline leverages this feature to perform microlocal pixelwise shrinkage and restore image quality without any assumption about noise uniformity [(C) and (D)]. (**E** to **H**) Siemens star images generated by simulating an average signal of 1 e^- (E), 3 e^- (F), 10 e^- (G), and 50 e^- (H) and corrupted by shot, readout, dark, and fixed-pattern noise. (**I** to **L**) MIRO-restored images corresponding to (E) to (H). (**M**) Image SNRs before (gray) and after (yellow) noise correction as a function of the average number of impinging photoelectrons per frame. Each point represents the average SNR measured over 100 simulated images. The solid lines are the relative best-fit curves obtained via polynomial regression. The dashed line represents the behavior of an ideal digital camera, i.e., only affected by Poisson shot noise. (**N** to **V**) MIRO restoration of fluorescent images of peroxisomes in human embryonic kidney (HEK) cells acquired using an EMCCD camera [(N) and (Q)], actin and mitochondria in bovine pulmonary artery endothelial (BPAE) cells acquired using an sCMOS camera [(O) and (R)], and microtubules in BPAE cells acquired using a PMT with the pinhole set at 0.25 AU [(P) and (S)]. [(T) to (V)] Corresponding cross-sectional profiles along the dashed lines marked in the (N) to (P) insets, respectively, exhibiting the recovery of image details and resolution by MIRO. Scale bars, 4 μm [(A), (E), and (N)], 10 μm (**O**), 1 μm [(N) inset, (O) inset, and (P)], and 500 nm [(P) inset].

to 3 μs), which may lead to severe photodamage and reduced acquisition speed (*33*). Here, we validated that MIRO effectively alleviates the limitation of PMT in photon collection while maintaining low laser power and fast pixel dwell time (~0.6 μs). Undistorted 3D LSCM data can be recovered despite the highly nonuniform photon shot noise, allowing for faster volumetric acquisition without compromising the sample health and underlying signal details (Fig. 2, I to L, movie S4, and fig. S4).

Notably, image restoration can also recover the functionality of conventional microscopy, otherwise hindered owing to the noise. In theory, LSCM can gain a $\sqrt{2}\times$ improvement in resolution over the diffraction limit with a pinhole closed well below 1 Airy Unit [AU, i.e., the size of the central lobe of the Airy disc (*32*)]. However, in

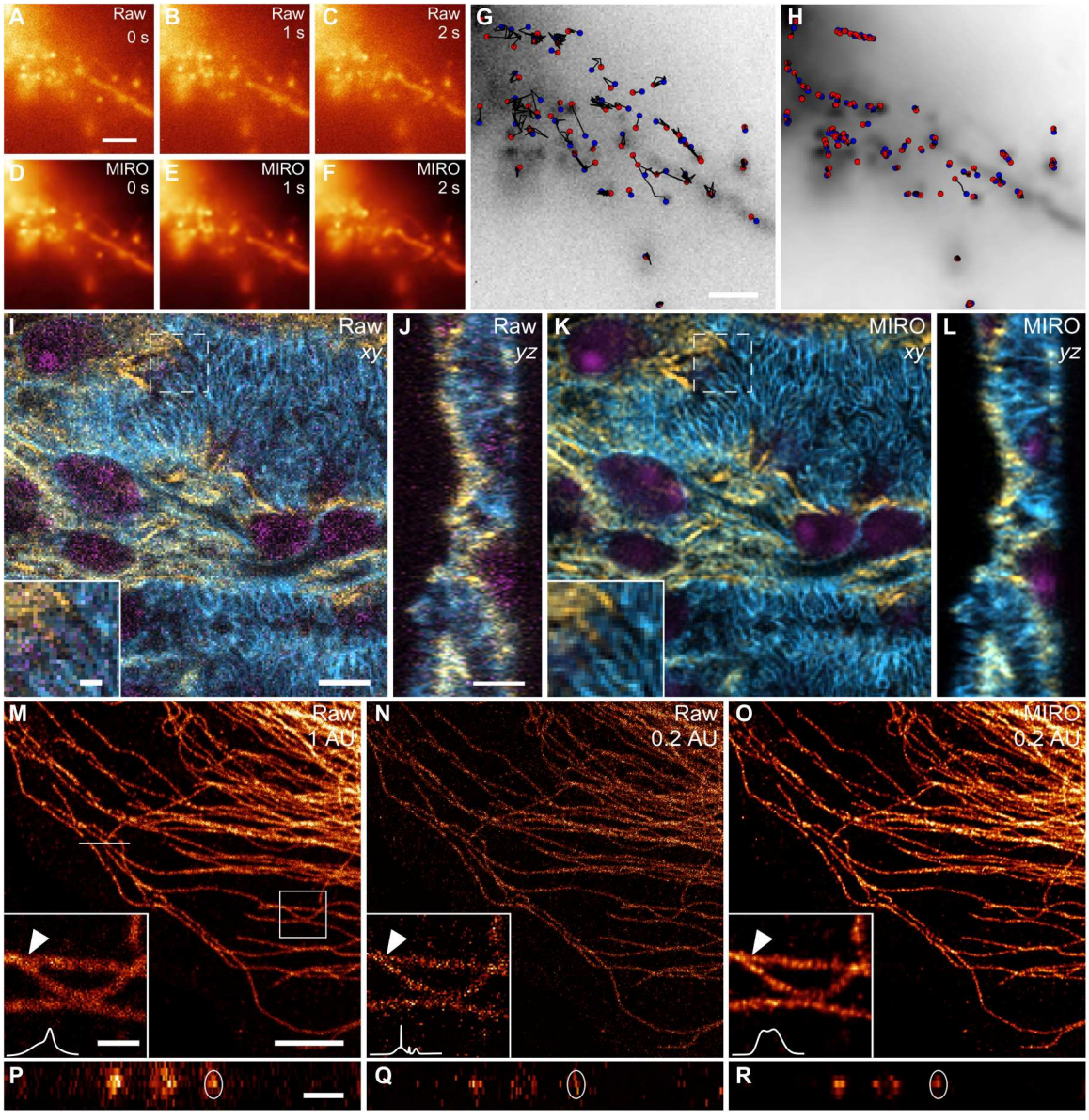

Fig. 2. MIRO processing enhances the data analysis and functionality of fluorescence microscopy. (**A** to **F**) Representative time-lapse frames of mitochondria in live HEK cells recorded at 50 Hz before (A) to (C) and after (D) to (F) MIRO processing. (**G** and **H**) Tracking individual mitochondria in the raw (G) and MIRO-processed (H) videos using Mitometer, showing substantially reduced misidentification. (**I** to **L**) Cross-sectional views in *xy* (I) and *yz* (J) and corresponding images recovered by MIRO [(K) and (L)] of a mouse kidney cryostat slice stained with 4′,6-diamidino-2-phenylindole (purple), phalloidin (orange), and wheat germ agglutinin (blue) imaged using a confocal microscope equipped with a standard PMT. (**M** and **N**) Immuno-stained microtubules of a BPAE cell acquired using a confocal microscope equipped with a GaAsP PMT at a consistent illumination level with the pinhole set to 1 AU (M) and 0.2 AU (N). (**O**) MIRO-processed image of (N), exhibiting an enhanced SNR comparable to (M) with substantially improved optical sectioning and subdiffraction-limited resolution due to the closed pinhole. The insets of (M) to (O) show the zoomed-in images of the corresponding boxed region as marked in (M), displaying arrow-marked filaments separated as close as 158 nm can be resolved in (O) (white cross-sectional profiles). (**P** to **R**) Cross-sectional images of (M) to (O) along the corresponding solid line as marked in (M), showing suppressed noise influence and improved FWHM measurements of the circled filament at 260 and 740 nm (P), 115 and 460 nm (Q), 158 and 344 nm (R) in the lateral and axial dimensions, respectively. The results in (R) obtained with MIRO processing are consistent with the expected resolution for a confocal microscope with a closed pinhole at 152 and 340 nm, respectively. Scale bars, 2 μm [(A) and (G)], 5 μm [(I), (J), and (M)], and 1 μm [(I), (M) insets, and (P)].

practice, the loss of signal and drastically elevated noise influence outpace the resolution gain (*31*). As a result, achieving this super-resolution capability requires alternative strategies such as image-scanning microscopy (*34*–*36*), which increases the instrument complexity. Using MIRO, we demonstrated its viability for obtaining subdiffraction-limited images from conventional LSCM using both standard and GaAsP PMTs (*33*). Specifically, as the pinhole was nearly closed below 0.25 AU, the noise level became detrimental to the image quality and effective resolution in both the lateral and axial dimensions (Fig. 2, M and N). In contrast, the MIRO-processed data at reduced pinholes not only displayed restored SNRs comparable to those generated through an open pinhole (1 AU) but also were benefitted from tighter pinholing and optical sectioning, leading to a noticeably improved rendering of cellular structures in all three dimensions (Fig. 2, O to R, movie S5, and figs. S5 to S7). The recovered results exhibited a subdiffraction-limited resolution consistent with the predicted values of ~150 nm (lateral) and ~340 nm (axial) for LSCM with a closed pinhole (Fig. 2, M to R), prompting a practicable 3D super-resolution functionality based on commonly available confocal systems.

Reduction of image reconstruction artifacts

Furthermore, the presence of noise produces artifacts and miscalculated biological information for microscopy techniques relying on computational processing (*1*, *37*, *38*). For this reason, MIRO can be instrumental in improving the processing pipeline of a broader range of computational microscopy techniques. For instance, using MIRO, we observed a noticeable reduction of noise-related artifacts and improved reliability of the processed image in deconvolution microscopy (*39*, *40*) (Fig. 3, A to D). Similarly, structured illumination microscopy (SIM) relies on image processing to achieve super-resolution but can be prone to spatially random reconstruction artifacts induced by low SNR (*41*) (Fig. 3E). Conventional approaches using Wiener deconvolution remain unable to fully suppress these artifacts while retaining the optimal resolution (*42*). On the contrary, we observed that postprocessing of SIM images by MIRO presented a considerable reduction of excessive random, noncontinuous artifacts while preserving the fine resolution of cellular details (Fig. 3, F to J, fig. S8, and movie S6). Notably, while other strategies for artifact minimization for SIM depend on a priori assumptions of either Poisson-distributed noise (*42*) or spatiotemporal continuity (*43*), MIRO showed an effective data recovery without posing such constraints (figs. S9 to S11).

Last, we verified MIRO noise correction for time-lapse functional imaging with Fourier light-field microscopy (FLFM, or extended LFM) (*44*–*47*). This emerging light-field approach computationally recovers biological sample volumes from scanning-free snapshot recording, achieving high spatiotemporal resolution with minimum photodamage per volumetric rendering (*48*–*52*). Nonetheless, the deconvolution-based reconstruction process is highly sensitive and may miscalculate 3D objects or cause computational artifacts due to a low image SNR. First, we conducted the time-lapse light-field observation of cardiac spheroids, 3D human-induced pluripotent stem cell–derived cardiomyocytes (hiPSC-CMs) that effectively recapitulate the human heart's cellular and extracellular microenvironment (*53*). As seen, the use of MIRO to facilitate light-field acquisition resulted in a remarkable improvement in differentiating every single cell across intact hiPSC-CMs (Fig. 3, K and L, and fig. S12). The enhanced results revealed the simultaneous morphological and functional variations of cardiomyocyte beating and Ca^{2+} transients in the volumetric spheroidal context (>350 μm by 350 μm by 240 μm per 10-ms acquisition), permitting longitudinal observation with low illumination for tens of thousands of time points and more accurate, volumetric characterization of the 3D cardiac spheroids (Fig. 3, M to T, fig. S13, movie S7, and table S2). Next, we observed the embryonic frog heart in vivo using FLFM. With MIRO, light-field imaging provides a clear visualization of the morphological changes between relaxation (diastole) and contraction (systole) of the ventricular chamber (Fig. 3, U to X, fig. S14, and movie S8), allowing for effective quantification of the embryonic heart function (table S3).

DISCUSSION

In conclusion, nowadays, image denoising and restoration in fluorescence microscopy demand quantitative accuracy, content compatibility, and platform generalizability. Despite numerous advances in the field, no physics-based solution has been demonstrated as robust and compatible with all major imaging systems. In this work, we presented MIRO as a system-aware solution based on microlocal noise correction with broad applicability to current microscopy platforms. This introduces the use of optimal sparsity in combination with physical modeling to allow for deterministic and sensor-agnostic recovery of noise-corrupted signals free from the knowledge of the target observed. Notably, the physical model is based on the approximation of the Poisson distribution to a heteroskedastic Gaussian to account for the spatially varying noise. This approximation introduces virtually no error already with $S = 10$ photons and is robust even at lower-photon regimes ($S \approx 3$–5 photons per pixel). These conditions on the photon flux are usually satisfied for many applications in fluorescence microscopy and, remarkably, we observed that MIRO restoration still yielded supraideal noise correction at even lower photon counts (<3 photons per pixel) with both simulation and experimental data. Moreover, we have validated the method with several imaging techniques (table S4) and found that MIRO restoration retains nominal microscopy resolution, facilitates downstream analysis, and enables otherwise impractical microscopy functionalities. For these reasons, we anticipate that MIRO would be a valuable toolkit to improve data visualization and processing pipelines in digital microscopy.

Furthermore, recently, another trending avenue for image denoising centered on learning-based approaches has been proven highly effective, given a comprehensive training database (*54*–*63*). In contrast, deterministic algorithms such as MIRO are readily accessible to diverse image data formats, can maintain the quantitative details of the signal, and become especially preferable for discovering biological knowledge beyond available training datasets (*64*). For this reason, hybrid strategies have lately been formulated to exploit the advantages of both worlds (*65*–*67*). In particular, it has been proposed that the shearlet transform of vast curvilinear biological features can effectively reduce the complexity of the learning problems, thus permitting more efficient convergence for network training (*68*). Extending the concept to the field of denoising, we anticipate that the MIRO framework could be feasibly synergized with existing learning-based algorithms to enhance the performance (section S3). As a proof of principle, we implemented a learnable shearlet shrinkage network that integrates shearlet

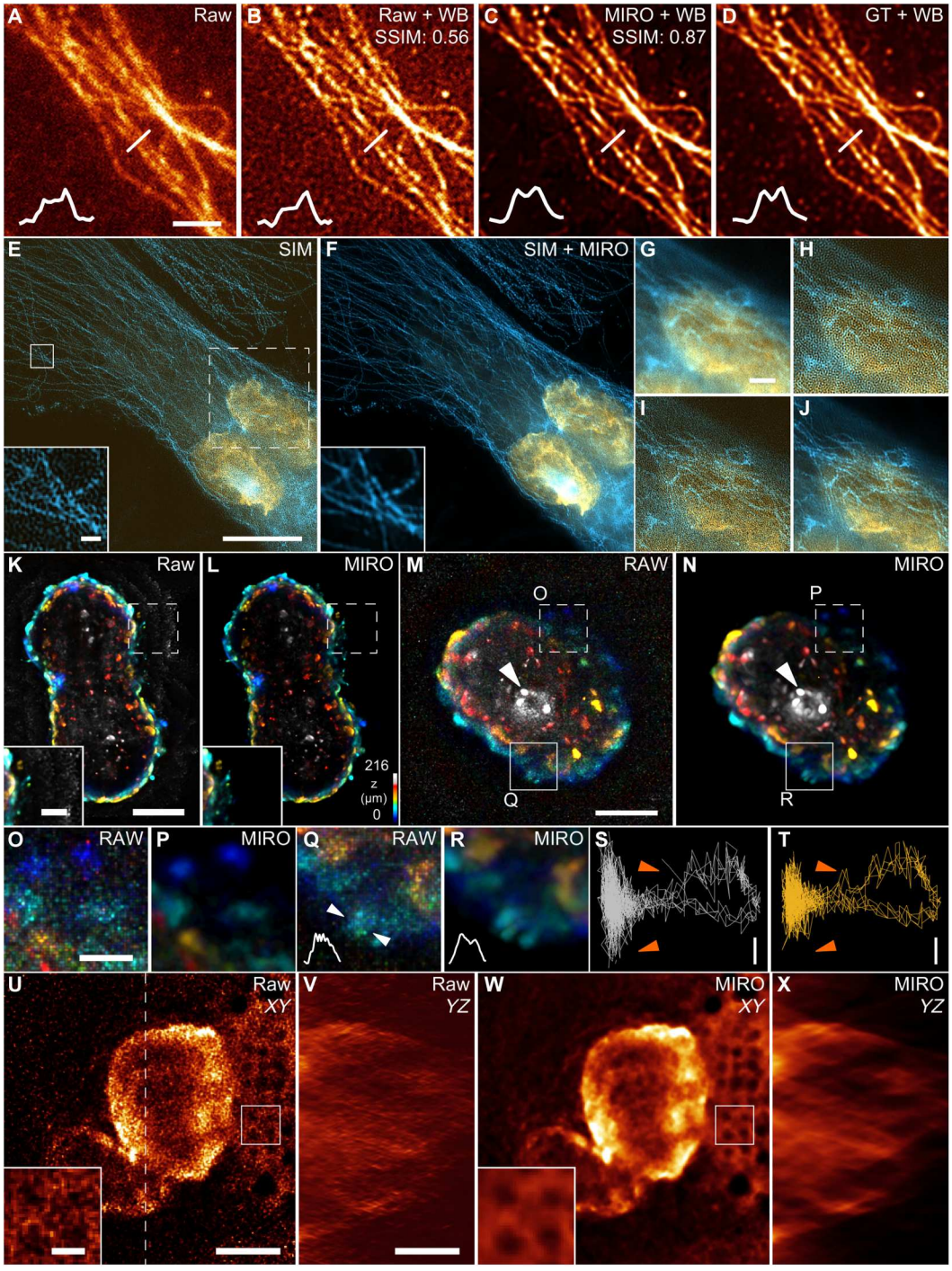

Fig. 3. MIRO minimizes image reconstruction artifacts. (**A**) Total internal reflection fluorescence images of immunostained microtubules in BPAE cells. (**B**) Wiener-Butterworth (WB) deconvolution of (A), showing nonfluorophore-related peaks. (**C**) WB deconvolution after MIRO processing shows closer similarity (SSIM, cross-sectional profiles) to the ground truth (GT) (**D**). The profiles' length is 1.4 μm. The peak-to-peak distance in (C) and (D) is 325 nm. (**E** and **F**) Original and MIRO-processed dual-color SIM image of microtubules (blue) and nuclei (orange) in BPAE cells. The insets correspond to the solid boxed region in (E). Compared with wide-field (**G**), high-pass wide-field (**H**), and SIM images (**I**), the MIRO-restored SIM reconstruction (**J**) shows a substantial artifact minimization. (**K**) 3D light-field reconstruction of membrane and calcium co-labeled cardiac spheroids. (**L**) The MIRO-processed reconstructions show a reduction of miscalculated 3D information and noise-related peaks [(K) and (L) insets]. (**M** and **N**) Light-field reconstruction of calcium-labeled cardiac spheroid without (M) and with (N) MIRO processing. (**O** to **R**) Zoom-ins corresponding to the boxed regions in (M) and (N). Depth is color-coded according to the bar in (L). (**S** and **T**) 3D beating trajectory of the cardiomyocyte indicated in (M) and (N). The trajectory from the MIRO-processed image (T) displays less fluctuations; see arrows in (S) and (T). (**U** to **X**) Light-field reconstruction of eGFP-labeled frog embryos without (u and v) and with (w and x) MIRO processing in XY (volume central slice) and YZ (along the dashed line) views. The insets show the ventricle and surrounding melanocytes (pigmentation) on the surface of the gut (boxed regions). Scale bars, 2 μm [(A), (S), and (T)], 10 μm (E), 500 nm [(E) inset], 100 μm [(K), (M), (U), and (V)], 30 μm [(K) inset and (O)], and 20 μm [(U) inset].

transform, system-aware parameters, and a customized MIRO-like U-Net (fig. S15A), with which we observed improved loss function minimization and convergence in comparison with the conventional U-Net for denoising tasks (section S3.3). We validated this hybrid concept by processing the 3D image datasets of single-cell and organoid specimens acquired with lattice light-sheet microscopy and confocal microscopy, respectively (figs. S15 and S16 and movie S9). Such hybrid implementation of deterministic models with deep learning will mitigate many constraints owing to the availability and quality of training data while enabling machine intelligence for those biological observations with insufficient knowledge. Similarly, we anticipate self-learnable frameworks (*39*) for image denoising fed with MIRO-processed datasets to further expand the efficiency and scope of the MIRO framework for broad biological imaging and discovery.

MATERIALS AND METHODS

Camera calibration

To calibrate the pixel-dependent noise of the CMOS cameras (ORCA-Flash-4.0 v3, Hamamatsu) used in this work, we followed the procedure previously reported in (*19*). Briefly, we recorded a series of dark images (10,000 frames) and then multiple sets of images with different illumination intensities ranging from ~20 to 500 photons per pixel. The offset, variance, and gain for each pixel were calculated using the relations as described in section S1.3. Notably, new tools have been recently developed that simplify this process allowing for automatic CMOS camera characterization (*69*).

Wide-field microscopy

Wide-field acquisitions were performed on an inverted optical microscope (Ti-U, Nikon). The lasers (MPB) were coupled into an optical fiber (Thorlabs) and sent to the microscope. We used an oil-immersion objective (CFI-PLAN Apo Lambda 100×/1.45, Nikon) to enable subcellular structure imaging. A lens with a focal length of 20 cm was used to focus the laser beam at the back focal plane of the objective. The lens could be moved to enable total internal reflection fluorescence illumination. The emitted fluorescence was collected with an sCMOS camera (ORCA-Flash-4.0 v3, Hamamatsu).

Microtubules were stained with mouse anti-Tom20 (F10, SC-17764, Santa Cruz Biotechnology) for 2 hours while gently shaking at room temperature. The second antibody was labeled with Alexa Fluor 647–conjugated AffiniPure Goat Anti-Mouse IgG (1 mg/ml; Jackson ImmunoResearch), followed by a 1-hour incubation at room temperature. A triple-washing step (5 min per wash) was conducted with phosphate-buffered saline (PBS) after each staining and labeling step. The cells were placed in an imaging buffer [1 M tris (pH 8.0), 5 M NaCl, 1.0 N HCl, cyclooctane (COT), cysteamine (MEA), and 50% glucose] before imaging.

Human embryonic kidney–293 [CRL-1573, American Type Culture Collection (ATCC)] cells were cultured at 5% CO_2 in Dulbecco's modified Eagle's medium (DMEM, Gibco) supplemented with 10% fetal bovine serum (FBS) and 1% penicillin-streptomycin. For mitochondrial imaging, cells were treated with MitoTracker Green (Invitrogen) at 100 nM for 30 min.

Commercially available prepared slides (FluoCells Slide no. 1 and no. 2, Thermo Fisher Scientific) were used to image mitochondria, F-actin, microtubules, and nuclei of bovine pulmonary artery endothelial (BPAE) cells. Mitochondria were labeled with red-fluorescent MitoTracker Red CMXRos, F-actin was stained with green-fluorescent Alexa Fluor 488 phalloidin (slide no. 1) or Texas Red-X phalloidin (slide no. 2), microtubules were stained with BODIPY FL, and nuclei were stained with 4′,6-diamidino-2-phenylindole (DAPI).

The 3D motion of peroxisomes in live HeLa cells was recorded using an inverted microscope equipped with a 63× objective lens (Plan-Apochromat 63×/1.40 DIC, Zeiss) and an EMCCD camera (Andor technologies). Hela cells (93021013, Sigma-Aldrich) for imaging were seeded on a poly-D-lysin–coated 35-mm dish (FD35PDL-100, World Precision Instruments) containing 3 ml of DMEM mixed with 10% FBS and 1% penicillin-streptomycin (Pen-Strep, 15140122, Thermo Fisher Scientific) at 37°C with 5% CO_2. When cells reached 80% confluency, they were rinsed twice with Hanks' balanced salt solution (HBSS) and then transfected in 3 ml of transfection buffer as a mixture of 3-ml modified DMEM and 50-μl peroxisome–green fluorescent protein (GFP) (CellLight C10604, Thermo Fisher Scientific). Imaging was taken after 1 day of incubation. At first, the transfection buffer was removed, and the cells were rinsed twice with HBSS. For live-cell imaging, 2 ml of Live Cell Imaging Solution (A14291DJ, Thermo Fisher Scientific) that was prewarmed to 37°C was added to the sample.

Confocal microscopy

A cryostat section of the mouse kidney (FluoCells slide no. 3, Thermo Fisher Scientific) was used to image nuclei (DAPI), F-actin (phalloidin), and microtubules (wheat germ agglutinin) with a confocal microscope (LSM 700, Zeiss). The microscope is equipped with a PMT, a 63× objective lens (Plan-Apochromat 63×/1.40, Zeiss), and four diode lasers, of which we used three (405, 488, and 555 nm). The pinhole was set to 1 AU.

To culture MCF10A mammary 3D organoids, MCF10A cells (ATCC) were seeded in a 384-well hanging drop culture plate (*70*–*72*). Three thousand MCF10A cells were seeded in each well at a final volume of 25 μl. The cells were supplemented with 0.24% methocel A4M (lot BCBR9701V, Sigma-Aldrich, no. 94378), 120 μg/ml Matrigel (10.7 mg/ml, lot 0337002, no. 256231, Corning), and 10% FBS (lot A52G00J, GemiBio no. 900-108). On day 3 of organoid culture, the organoids were collected and fixed in 4% paraformaldehyde for 30 min at room temperature. The organoids were washed three times with PBS and kept at 4°C until imaging analysis. For confocal imaging, the fixed organoids were permeabilized with 0.5% Triton X-100 (lot SLBV4122, Sigma-Aldrich, no. T8787) for 30 min at room temperature. The organoids were washed three times with PBS and added Phalloidin Alexa 488 (diluted 1:40, no. A12379, Invitrogen) and incubated for 30 min. The organoids were washed with PBS and added Hoechst 33342 (10 mg/ml, 1:5000, no. H3570, Invitrogen) and incubated for 20 min. After washing with PBS, they were transferred to the 35-mm MatTek plate (P35G-1.5-14-C, No.1.5 cover glass) and mounted with 1% low melting agarose (no. A0701, Sigma-Aldrich).

Fluorescently stained microtubules of BPAE cells (FluoCells slide no. 2, Thermo Fisher Scientific) were used to test subdiffraction-limited confocal imaging. The datasets acquired with the standard PMT were obtained using a Zeiss LSM 700 equipped with a 63× objective lens (Plan-Apochromat 63×/1.40, Zeiss) and with the pinhole set to 0.25 AU. The datasets acquired with the GaAsP-PMT were obtained using a Zeiss LSM 780 microscope

with a 100× objective lens (Plan-Apochromat 100×/1.46 Oil DIC, Zeiss) and the pinhole set to 0.2 AU. The diffraction-limited reference images were acquired by setting the pinhole size to 1 AU. In both cases, the sample was illuminated using a 25-mW Argon laser with the transmittance set to 2% for an effective laser power of 500 μW.

Structured illumination microscopy

Dual-color SIM imaging was performed on a Zeiss Elyra inverted fluorescence microscope equipped with an EMCCD camera (Andor technologies). The images were acquired using a 63× objective lens (Plan-Apochromat 63×/1.40 DIC, Zeiss). Each super-resolution image was reconstructed from 15 images acquired at three different angles with five different phases per angle. SIM reconstructions were performed using fairSIM (*73*).

Fourier light-field microscopy

hiPSCs (WiCell Research Institute) were maintained mTeSR1 medium (STEMCELL Technologies) and induced for cardiac differentiation as previously described in (*74*). Briefly, hiPSCs cells were treated with recombinant human activin A (100 ng/ml; R&D Systems) in RPMI medium with 2% B27 insulin-free (RPMI/B27 insulin-free medium) on day 0. After 24 hours, the medium was replaced with recombinant human bone morphogenic protein–4 (10 ng/ml; R&D Systems) in RPMI/B27 insulin-free medium from day 1 to day 4. The medium was changed to RPMI medium with 2% B27 containing insulin (RPMI/B27 medium) on day 4.

Cardiac spheres were generated on differentiation day 5 using the procedure described in (*74*). Differentiated cells were dissociated with 0.25% trypsin/EDTA and seeded into AggreWell 400 plates (no. 34415, STEMCELL Technologies) at 1500 cells per microwell to allow cells to form cardiac spheres. Before cell seeding, plates with 1 ml per well of RPMI/B27 medium were centrifuged at 1000*g* to release trapped bubbles in microwells. To prevent cell death, the medium was supplemented with 10 μM Rock inhibitor Y-27632 (Selleck Chemicals). Plates were centrifuged at 100*g* to distribute the cells and then placed in an incubator. After 24 hours, spheres were harvested to remove the Rock inhibitor, and RPMI/B27 medium was replaced in the suspension culture. 3D spheroids were maintained until the day of testing <30 days after differentiation. Medium was changed every 2 days.

For membrane staining of cardiac spheres, the culture medium was replaced with the culture medium loaded with a 200-μl GFP labeling medium (CellLight Nucleus-GFP, BacMam 2.0, Thermo Fisher Scientific). On the day of imaging, the staining solution was made by adding 4.56 μl of anhydrous dimethyl sulfoxide (DMSO) (D12345, Thermo Fisher Scientific) into one vial of Fluo-4 AM (F14201, Thermo Fisher Scientific) and diluting it into 4.56 ml of prewarmed maturation medium to reach a final concentration of 10 μM. Then, the original maturation medium of the cells was replaced by the fresh culture medium loaded with Fluo-4 AM, and the cells were incubated in the incubator for 45 min. After that, the staining medium was replaced by 3 ml of 1X Normal Tyrode [126 mM NaCl (Sigma-Aldrich, S9625-500G), 4 mM KCl (Sigma-Aldrich, 793590-500G), 1 mM $MgCl_2$ (Sigma-Aldrich, 63069-100 mL), and 5 mM Hepes (Sigma-Aldrich, H0887-100 mL), pH adjusted to 7.4 with 1 M NaOH] with extra 10 mM D-Glucose (Sigma-Aldrich, G7528-250G), and 1.8 mM $CaCl_2$ (Sigma-Aldrich, 21115), and the cells were incubated for 10 min. In the end, the Tyrode was aspirated, and cells were incubated in a 3 ml prewarmed maturation medium for over 30 min for recovery. For spheroids used in Fig. 3 (M and N), the staining solution was made by mixing one vial of Fluo-4 AM (F14201, Thermo Fisher Scientific) with 45.6 μl anhydrous DMSO (D12345, Thermo Fisher Scientific) and diluting 5 μl of the mixture by 1000× with 495 μl Normal Tyrode. Then, the cells were incubated in the staining solution for 45 min and then washed with 1× Normal Tyrode for 10 min at 37°C.

Transgenic embryos of *Xenopus laevis* were obtained by fertilizing wild-type oocytes with myl3:eGFP testis (ordered from the National Xenopus Resource). The fertilized embryos were screened for fluorescent signals in the heart and raised to stage as described in (*75*). The tadpoles were then mounted ventral side up on an agarose bed in 0.1× Marc's Modified Rinders (MMR) plus 0.1% MS222, gently secured under a piece of cover glass. All experimental procedures were performed according to U.S. Department of Agriculture Animal Welfare Act Regulations and have been approved by Institutional Animal Care and Use Committee in compliance with Public Health Service Policy.

The specimens were imaged using a homemade FLFM system equipped with a water-dipping physiology objective lens (CFI75 LWD 16×/0.8 W, Nikon) and used a 300-mm tube lens (AC508–300-A-ML, Thorlabs), a 200-mm Fourier lens (AC508–200-A-ML, Thorlabs), and a customized microlens array MLA that consists 3 by 3 planoconvex lenses which are 3.3 mm square with 30-mm focal length as described in (*50*). The sample was illuminated with a light-emitting diode (LED) peaked at 470 nm (M470L5, Thorlabs), and a filter set (89402-ET-391-32/479-33/554-24/638-31 Multi LED set, Chroma) was adopted. Videos were recorded on an sCMOS camera (ORCA-Flash-4.0 v3, Hamamatsu) at a frame rate of 100 Hz.

Lattice light-sheet microscopy

Lattice light-sheet microscopy images were acquired using a 3i Lattice Light Sheet microscope. Here, lasers are individually expanded in the laser launch to 2.5 mm, collimated, and aligned to be co-linear. All lines pass through an acousto-optic tunable filter that regulates the laser power input into the system. Then, a set of cylindrical lenses expands the 2.5-mm input beam to uniformly illuminate a stripe on the spatial light modulator (SLM). This is programmed to display binary images of multi-Bessel patterns that form an optical lattice of Bessel beams. This is projected onto an annular mask, which filters the zeroth order, removes artifacts, and lengthens the sheet. The mask is serially conjugate to z and x galvo mirrors, as well as the rear pupil of the excitation objective, allowing the light sheet to be translated in y and z and to rapidly oscillate in x for the dithered mode of operation. The beam is focused through the illumination objective to create a pattern of the Bessel beams at the sample plane that is conjugate to the projection of the SLM. This pattern is dithered by the x galvo to form the sheet of illumination. The fluorescence emitted by the sample is observed by the sCMOS camera (ORCA-Flash4.0 v2, Hamamatsu) through the detection optics, which are composed by a 1.1–numerical aperture (NA) water objective and a 500-nm tube lens for a ×62.5 total magnification.

The volumetric data acquisition was performed in the sample scan modality. Here, the stage moves while the light sheet and the objectives remain stationary. This mode allows for scanning

extensive areas, but because the objective is tilted at an angle with respect to the axis of stage movement, the scan produces a lateral offset between images from neighboring z planes. Therefore, these images are shifted (or deskewed) in postprocessing to retrieve the original positions. To maintain the 3D information of the sample, we performed our denoising only after deskewing.

HaCaT keratinocytes were generously provided by Kowalczyk Lab at Emory University. They were cultured in DMEM (Corning, Tewksbury, MA) supplemented with 10% FBS and 1% antibiotic/antimycotic. Cells grown on 5-mm coverslips were transfected according to the manufacturer's instruction with Viromer RED (OriGene, Rockville, MA). Briefly, plasmids were incubated with Viromer RED transfection reagent and buffer for 20 min at room temperature. This plasmid/reagent mix was then added to cells in culture dishes. Cells were then fixed 24 hours after transfection with 4% paraformaldehyde for 15 min. The mCherry-VAPB (human) plasmid construct was purchased from Addgene (Plasmid no. 108126).

Simulations

To characterize MIRO denoising performance, we have used three different simulated fluorescence image datasets depicting a Siemens star, fluorescent beads, and microtubules. In all cases, we have generated images using the following parameters: NA 1.45, wavelength 680 nm, and pixel size 65 nm. The noisy images were generated by corrupting the signal with fixed-pattern noise, photon shot noise, dark shot noise, and readout noise.

Supplementary Materials

This PDF file includes:
Sections S1 to S3
Figs. S1 to S35
Tables S1 to S7
Legends for movies S1 to S9
Legend for supplementary software file
References

Other Supplementary Material for this manuscript includes the following:
Movies S1 to S9
Supplementary software file

REFERENCES AND NOTES

1. A. P.-T. Jost, J. C. Waters, Designing a rigorous microscopy experiment: Validating methods and avoiding bias. *J. Cell Biol.* **218**, 1452–1466 (2019).
2. N. Scherf, J. Huisken, The smart and gentle microscope. *Nat. Biotechnol.* **33**, 815–818 (2015).
3. A. R. Hibbs, G. MacDonald, K. Garsha, "Practical confocal microscopy" in *Handbook Of Biological Confocal Microscopy*, J. B. Pawley, Ed. (Springer, 2006), chap. 36, pp. 650–671.
4. J. Icha, M. Weber, J. C. Waters, C. Norden, Phototoxicity in live fluorescence microscopy, and how to avoid it. *Bioessays* **39**, 1700003 (2017).
5. P. P. Laissue, R. A. Alghamdi, P. Tomancak, E. G. Reynaud, H. Shroff, Assessing phototoxicity in live fluorescence imaging. *Nat. Methods* **14**, 657–661 (2017).
6. J. C. Waters, Accuracy and precision in quantitative fluorescence microscopy. *J. Cell Biol.* **185**, 1135–1148 (2009).
7. J. R. Janesick, *Photon Transfer* (SPIE, 2007).
8. A. Buades, B. Coll, J.-M. Morel, Image Denoising Methods. A New Nonlocal Principle. *SIAM Review* **52**, 113–147 (2010).
9. K. Dabov, A. Foi, V. Katkovnik, K. Egiazarian, "Image denoising with block-matching and 3D filtering" in *Image Processing: Algorithms and Systems, Neural Networks, and Machine Learning*, E. R. Dougherty, J.Y. Astola, K. O. Egiazarian, N. M. Nasrabadi, S. A. Rizvi, Eds. (SPIE, 2006), vol. 6064, p. 606414.
10. R. C. Gonzalez, R. E. Woods, B. R. Masters, Digital image processing (Pearson, 2008).
11. L. Azzari, A. Foi, Variance stabilization for Noisy+estimate combination in iterative poisson denoising. *IEEE Signal Process. Lett.* **23**, 1086–1090 (2016).
12. A. A. Bindilatti, N. D. A. Mascarenhas, A nonlocal poisson denoising algorithm based on stochastic distances. *IEEE Signal Process. Lett.* **20**, 1010–1013 (2013).
13. F. Luisier, T. Blu, M. Unser, Image denoising in mixed Poisson–Gaussian noise. *IEEE Trans. Image Process.* **20**, 696–708 (2011).
14. W. Meiniel, J.-C. Olivo-Marin, E. D. Angelini, Denoising of microscopy images: A review of the state-of-the-art, and a new sparsity-based method. *IEEE Trans. Image Process.* **27**, 3842–3856 (2018).
15. J. M. Murray, "Practical Aspects of Quantitative Confocal Microscopy" in *Digital Microscopy*, G. Sluder, D. E. Wolf, Eds. (Academic Press, 2007), pp. 467–478.
16. F. Huang, T. M. Hartwich, F. E. Rivera-Molina, Y. Lin, W. C. Duim, J. J. Long, P. D. Uchil, J. R. Myers, M. A. Baird, W. Mothes, M. W. Davidson, D. Toomre, J. Bewersdorf, Video-rate nanoscopy using sCMOS camera-specific single-molecule localization algorithms. *Nat. Methods* **10**, 653–658 (2013).
17. P. Coupé, M. Munz, J. V. Manjon, E. S. Ruthazer, D. L. Collins, A CANDLE for a deeper in vivo insight. *Med. Image Anal.* **16**, 849–864 (2012).
18. S. Liu, M. J. Mlodzianoski, Z. Hu, Y. Ren, K. McElmurry, D. M. Suter, F. Huang, sCMOS noise-correction algorithm for microscopy images. *Nat. Methods* **14**, 760–761 (2017).
19. B. Mandracchia, X. Hua, C. Guo, J. Son, T. Urner, S. Jia, Fast and accurate sCMOS noise correction for fluorescence microscopy. *Nat. Commun.* **11**, 94 (2020).
20. J. He, Y. Cai, J. Wu, Q. Dai, Spatial-temporal low-rank prior for low-light volumetric fluorescence imaging. *Opt. Express* **29**, 40721–40733 (2021).
21. G. Kutyniok, W.-Q. Lim, Compactly supported shearlets are optimally sparse. *J. Approx. Theory* **163**, 1564–1589 (2011).
22. W. Q. Lim, The discrete shearlet transform: a new directional transform and compactly supported shearlet frames. *IEEE Trans. Image Process.* **19**, 1166–1180 (2010).
23. G. R. Easley, D. Labate, "Image processing using shearlets" in *Shearlets*, G. Kutyniok, D. Labate, Eds. (Springer, 2012), pp. 283–325.
24. D. Labate, F. Laezza, P. Negi, B. Ozcan, M. Papadakis, Efficient processing of fluorescence images using directional multiscale representations. *Math. Model Nat. Phenom.* **9**, 177–193 (2014).
25. K. Guo, D. Labate, Optimally sparse multidimensional representation using shearlets. *SIAM J. Math. Anal.* **39**, 298–318 (2007).
26. G. R. Easley, D. Labate, F. Colonna, Shearlet-based total variation diffusion for denoising. *IEEE Trans. Image Process.* **18**, 260–268 (2009).
27. H. R. Shahdoosti, O. Khayat, Image denoising using sparse representation classification and non-subsampled shearlet transform. *Signal, Image and Video Process.* **10**, 1081–1087 (2016).
28. M. M. Frigault, J. Lacoste, J. L. Swift, C. M. Brown, Live-cell microscopy - tips and tools. *J. Cell Sci.* **122**, 753–767 (2009).
29. A. Ettinger, T. Wittmann, Fluorescence live cell imaging. *Methods Cell Biol.* **123**, 77–94 (2014).
30. A. E. Y. T. Lefebvre, D. Ma, K. Kessenbrock, D. A. Lawson, M. A. Digman, Automated segmentation and tracking of mitochondria in live-cell time-lapse images. *Nat. Methods* **18**, 1091–1102 (2021).
31. J. A. Conchello, J. W. Lichtman, Optical sectioning microscopy. *Nat. Methods* **2**, 920–931 (2005).
32. J. Pawley, *Handbook of Biological Confocal Microscopy* (Science & Business Media, 2006), vol. 236.
33. J. Jonkman, C. M. Brown, G. D. Wright, K. I. Anderson, A. J. North, Tutorial: Guidance for quantitative confocal microscopy. *Nat. Protoc.* **15**, 1585–1611 (2020).
34. C. J. Sheppard, S. B. Mehta, R. Heintzmann, Superresolution by image scanning microscopy using pixel reassignment. *Opt. Lett.* **38**, 2889–2892 (2013).
35. C. B. Müller, J. Enderlein, Image scanning microscopy. *Phys. Rev. Lett.* **104**, 198101 (2010).
36. Y. Wu, H. Shroff, Faster, sharper, and deeper: Structured illumination microscopy for biological imaging. *Nat. Methods* **15**, 1011–1019 (2018).
37. J. M. Heddleston, J. S. Aaron, S. Khuon, T.-L. Chew, A guide to accurate reporting in digital image acquisition - can anyone replicate your microscopy data? *J. Cell Sci.* **134**, jcs254144 (2021).
38. C. Karras, M. Smedh, R. Förster, H. Deschout, J. Fernandez-Rodriguez, R. Heintzmann, Successful optimization of reconstruction parameters in structured illumination microscopy – A practical guide. *Opt. Commun.* **436**, 69–75 (2019).
39. M. Guo, Y. Li, Y. Su, T. Lambert, D. D. Nogare, M. W. Moyle, L. H. Duncan, R. Ikegami, A. Santella, I. Rey-Suarez, D. Green, A. Beiriger, J. Chen, H. Vishwasrao, S. Ganesan,

V. Prince, J. C. Waters, C. M. Annunziata, M. Hafner, W. A. Mohler, A. B. Chitnis, A. Upadhyaya, T. B. Usdin, Z. Bao, D. Colón-Ramos, P. La Riviere, H. Liu, Y. Wu, H. Shroff, Rapid image deconvolution and multiview fusion for optical microscopy. *Nat. Biotechnol.* **38**, 1337–1346 (2020).

40. N. Gustafsson, S. Culley, G. Ashdown, D. M. Owen, P. M. Pereira, R. Henriques, Fast live-cell conventional fluorophore nanoscopy with ImageJ through super-resolution radial fluctuations. *Nat. Commun.* **7**, 12471 (2016).
41. G. Ball, J. Demmerle, R. Kaufmann, I. Davis, I. M. Dobbie, L. Schermelleh, SIMcheck: A toolbox for successful super-resolution structured illumination microscopy. *Sci. Rep.* **5**, 15915 (2015).
42. C. S. Smith, J. A. Slotman, L. Schermelleh, N. Chakrova, S. Hari, Y. Vos, C. W. Hagen, M. Müller, W. van Cappellen, A. B. Houtsmuller, J. P. Hoogenboom, S. Stallinga, Structured illumination microscopy with noise-controlled image reconstructions. *Nat. Methods* **18**, 821–828 (2021).
43. X. Huang, J. Fan, L. Li, H. Liu, R. Wu, Y. Wu, L. Wei, H. Mao, A. Lal, P. Xi, L. Tang, Y. Zhang, Y. Liu, S. Tan, L. Chen, Fast, long-term, super-resolution imaging with Hessian structured illumination microscopy. *Nat. Biotechnol.* **36**, 451–459 (2018).
44. A. Llavador, J. Sola-Pikabea, G. Saavedra, B. Javidi, M. Martínez-Corral, Resolution improvements in integral microscopy with Fourier plane recording. *Opt. Express* **24**, 20792–20798 (2016).
45. L. Cong, Z. Wang, Y. Chai, W. Hang, C. Shang, W. Yang, L. Bai, J. Du, K. Wang, Q. Wen, Rapid whole brain imaging of neural activity in freely behaving larval zebrafish (Danio rerio). *eLife* **6**, e28158 (2017).
46. G. Scrofani, J. Sola-Pikabea, A. Llavador, E. Sanchez-Ortiga, J. C. Barreiro, G. Saavedra, J. Garcia-Sucerquia, M. Martínez-Corral, FIMic: Design for ultimate 3D-integral microscopy of in-vivo biological samples. *Biomed. Opt. Express* **9**, 335–346 (2018).
47. C. Guo, W. Liu, X. Hua, H. Li, S. Jia, Fourier light-field microscopy. *Opt. Express* **27**, 25573–25594 (2019).
48. K. Yanny, N. Antipa, W. Liberti, S. Dehaeck, K. Monakhova, F. L. Liu, K. Shen, R. Ng, L. Waller, Miniscope3D: Optimized single-shot miniature 3D fluorescence microscopy. *Light Sci. Appl.* **9**, 171 (2020).
49. Y. Xue, I. G. Davison, D. A. Boas, L. Tian, Single-shot 3D wide-field fluorescence imaging with a Computational Miniature *Mesoscope*. *Sci. Adv.* **6**, eabb7508 (2020).
50. W. Liu, G.-A. R. Kim, S. Takayama, S. Jia, Fourier light-field imaging of human organoids with a hybrid point-spread function. *Biosens. Bioelectron.* **208**, 114201 (2022).
51. Z. Zhang, L. Bai, L. Cong, P. Yu, T. Zhang, W. Shi, F. Li, J. Du, K. Wang, Imaging volumetric dynamics at high speed in mouse and zebrafish brain with confocal light field microscopy. *Nat. Biotechnol.* **39**, 74–83 (2021).
52. X. Hua, W. Liu, S. Jia, High-resolution Fourier light-field microscopy for volumetric multi-color live-cell imaging. *Optica* **8**, 614–620 (2021).
53. D. C. Nguyen, T. A. Hookway, Q. Wu, R. Jha, M. K. Preininger, X. Chen, C. A. Easley, P. Spearman, S. R. Deshpande, K. Maher, M. B. Wagner, T. C. McDevitt, C. Xu, Microscale generation of cardiospheres promotes robust enrichment of cardiomyocytes derived from human pluripotent stem cells. *Stem Cell Reports* **3**, 260–268 (2014).
54. D. M. Camacho, K. M. Collins, R. K. Powers, J. C. Costello, J. J. Collins, Next-generation machine learning for biological networks. *Cell* **173**, 1581–1592 (2018).
55. E. Moen, D. Bannon, T. Kudo, W. Graf, M. Covert, D. Van Valen, Deep learning for cellular image analysis. *Nat. Methods* **16**, 1233–1246 (2019).
56. B. Midtvedt, S. Helgadottir, A. Argun, J. Pineda, D. Midtvedt, G. Volpe, Quantitative digital microscopy with deep learning. *Appl. Phys. Rev.* **8**, 011310 (2021).
57. M. Weigert, U. Schmidt, T. Boothe, A. Müller, A. Dibrov, A. Jain, B. Wilhelm, D. Schmidt, C. Broaddus, S. Culley, M. Rocha-Martins, F. Segovia-Miranda, C. Norden, R. Henriques, M. Zerial, M. Solimena, J. Rink, P. Tomancak, L. Royer, F. Jug, E. W. Myers, Content-aware image restoration: Pushing the limits of fluorescence microscopy. *Nat. Methods* **15**, 1090–1097 (2018).
58. J. Chen, H. Sasaki, H. Lai, Y. Su, J. Liu, Y. Wu, A. Zhovmer, C. A. Combs, I. Rey-Suarez, H.-Y. Chang, C. C. Huang, X. Li, M. Guo, S. Nizambad, A. Upadhyaya, S.-J. J. Lee, L. A. G. Lucas, H. Shroff, Three-dimensional residual channel attention networks denoise and sharpen fluorescence microscopy image volumes. *Nat. Methods* **18**, 678–687 (2021).
59. J. Lehtinen, J. Munkberg, J. Hasselgren, S. Laine, T. Karras, M. Aittala, T. Aila, Noise2noise: Learning image restoration without clean data. arXiv:1803.04189 [cs.CV] (12 March 2018).
60. Y. Wang, H. Pinkard, E. Khwaja, S. Zhou, L. Waller, B. Huang, Image denoising for fluorescence microscopy by supervised to self-supervised transfer learning. *Opt. Express* **29**, 41303–41312 (2021).
61. L. von Chamier, R. F. Laine, J. Jukkala, C. Spahn, D. Krentzel, E. Nehme, M. Lerche, S. Hernández-Pérez, P. K. Mattila, E. Karinou, S. Holden, A. C. Solak, A. Krull, T.-O. Buchholz, M. L. Jones, L. A. Royer, C. Leterrier, Y. Shechtman, F. Jug, M. Heilemann, G. Jacquemet, R. Henriques, Democratising deep learning for microscopy with ZeroCostDL4Mic. *Nat. Commun.* **12**, 2276 (2021).
62. R. F. Laine, G. Jacquemet, A. Krull, Imaging in focus: An introduction to denoising bioimages in the era of deep learning. *Int. J. Biochem. Cell Biol.* **140**, 106077 (2021).
63. V. Mannam, Y. Zhang, Y. Zhu, E. Nichols, Q. Wang, V. Sundaresan, S. Zhang, C. Smith, P. W. Bohn, S. S. Howard, Real-time image denoising of mixed Poisson–Gaussian noise in fluorescence microscopy images using ImageJ. *Optica* **9**, 335–345 (2022).
64. C. Belthangady, L. A. Royer, Applications, promises, and pitfalls of deep learning for fluorescence image reconstruction. *Nat. Methods* **16**, 1215–1225 (2019).
65. E. Bostan, R. Heckel, M. Chen, M. Kellman, L. Waller, Deep phase decoder: Self-calibrating phase microscopy with an untrained deep neural network. *Optica* **7**, 559–562 (2020).
66. Y. Li, Y. Su, M. Guo, X. Han, J. Liu, H. D. Vishwasrao, X. Li, R. Christensen, T. Sengupta, M. W. Moyle, J. Chen, T. B. Usdin, D. Colón-Ramos, H. Liu, Y. Wu, H. Shroff, Incorporating the image formation process into deep learning improves network performance in deconvolution applications. bioRxiv 2022.03.05.483139 [Preprint]. 6 March 2022. https://doi.org/10.1101/2022.03.05.483139.
67. H. Hermessi, O. Mourali, E. Zagrouba, Convolutional neural network-based multimodal image fusion via similarity learning in the shearlet domain. *Neural. Comput. Appl.* **30**, 2029–2045 (2018).
68. H. Andrade-Loarca, G. Kutyniok, tfShearlab: The TensorFlow Digital Shearlet Transform for Deep Learning. arXiv:2006.04591 [eess.IV] (8 June 2020).
69. R. Diekmann, J. Deschamps, Y. Li, T. Deguchi, A. Tschanz, M. Kahnwald, U. Matti, J. Ries, Photon-free (s)CMOS camera characterization for artifact reduction in high- and super-resolution microscopy. *Nat. Commun.* **13**, 3362 (2022).
70. S. I. Djomehri, B. Burman, M. E. Gonzalez, S. Takayama, C. G. Kleer, A reproducible scaffold-free 3D organoid model to study neoplastic progression in breast cancer. *J. Cell Commun. Signal* **13**, 129–143 (2019).
71. S. Lee, J. Chang, S. M. Kang, E. Parigoris, J.-H. Lee, Y. S. Huh, S. Takayama, High-throughput formation and image-based analysis of basal-in mammary organoids in 384-well plates. *Sci. Rep.* **12**, 317 (2022).
72. E. Parigoris, S. Lee, D. Mertz, M. Turner, A. Y. Liu, J. Sentosa, S. Djomehri, H. C. Chang, K. Luker, G. Luker, C. G. Kleer, S. Takayama, Cancer cell invasion of mammary organoids with basal-In phenotype. *Adv. Healthc. Mater.* **10**, e2000810 (2021).
73. M. Müller, V. Mönkemöller, S. Hennig, W. Hübner, T. Huser, Open-source image reconstruction of super-resolution structured illumination microscopy data in ImageJ. *Nat. Commun.* **7**, 10980 (2016).
74. R. Jha, Q. Wu, M. Singh, M. K. Preininger, P. Han, G. Ding, H. C. Cho, H. Jo, K. O. Maher, M. B. Wagner, C. Xu, Simulated microgravity and 3D culture enhance induction, viability, proliferation and differentiation of cardiac progenitors from human pluripotent stem cells. *Sci. Rep.* **6**, 30956 (2016).
75. S. J. Smith, P. Ataliotis, S. Kotecha, N. Towers, D. B. Sparrow, T. J. Mohun, The MLC1v gene provides a transgenic marker of myocardium formation within developing chambers of the Xenopus heart. *Dev. Dyn.* **232**, 1003–1012 (2005).
76. J. R. Janesick, Photon transfer noise sources, in *Photon Transfer*, J. R. Janesick, Ed. (SPIE, 2009), pp. 21–34.
77. J. R. Janesick, Photon transfer theory, in *Photon Transfer*, J. R. Janesick, Ed. (SPIE, 2009), pp. 35–48.
78. A. Foi, M. Trimeche, V. Katkovnik, K. Egiazarian, Practical Poissonian-Gaussian noise modeling and fitting for single-image raw-data. *IEEE Trans. Image Process.* **17**, 1737–1754 (2008).
79. H. T. Beier, B. L. Ibey, Experimental comparison of the high-speed imaging performance of an EM-CCD and sCMOS camera in a dynamic live-cell imaging test case. *PLOS ONE* **9**, e84614 (2014).
80. B. Moomaw, Camera technologies for low light imaging: Overview and relative advantages. *Methods Cell Biol.* **114**, 243–283 (2013).
81. G. D. Boreman, Transfer function techniques, in *Handbook of Optics*, M. Bass, Ed. (McGraw-Hill, 1995), pp. 1–10.
82. W. K. Pratt, *Introduction to Digital Image Processing* (CRC Press, 2018).
83. M. Colom, A. Buades, J.-M. Morel, Nonparametric noise estimation method for raw images. *J. Opt. Soc. Am. A* **31**, 863–871 (2014).
84. G. R. Easley, D. Labate, W. Q. Lim, Optimally sparse image representations using shearlets. *Conference Record - Asilomar Conference on Signals, Systems and Computers* (2006), pp. 974–978.
85. V. M. Patel, G. R. Easley, D. M. Healy, Shearlet-based deconvolution. *EEE Trans Image Process.* **18**, 2673–2685 (2009).
86. G. Kutyniok, W.-Q. Lim, Image separation using wavelets and shearlets, in *Curves and Surfaces*, J.-D. Boissonnat, P. Chenin, A. Cohen, C. Gout, T. Lyche, M.-L. Mazure, L. Schumaker, Eds. (Springer, 2012), vol. 6920, pp. 416–430.
87. G. Easley, D. Labate, W.-Q. Lim, Sparse directional image representations using the discrete shearlet transform. *Appl. Comput. Harmon. Anal.* **25**, 25–46 (2008).

88. A. Descloux, K. S. Grußmayer, A. Radenovic, Parameter-free image resolution estimation based on decorrelation analysis. *Nat. Methods* **16**, 918–924 (2019).
89. K. Dabov, A. Foi, V. Katkovnik, K. Egiazarian, Image restoration by sparse 3D transform-domain collaborative filtering. *Image Processing: Algorithms and Systems VI* **6812**, 681207 (2008).
90. A. Danielyan, V. Katkovnik, K. Egiazarian, Deblurring of Poissonian images using BM3D frames. *Wavelets and Sparsity XIV* **8138**, 813812 (2011).
91. P. M. Carlton, J. Boulanger, C. Kervrann, J. B. Sibarita, J. Salamero, S. Gordon-Messer, D. Bressan, J. E. Haber, S. Haase, L. Shao, L. Winoto, A. Matsuda, P. Kner, S. Uzawa, M. Gustafsson, Z. Kam, D. A. Agard, J. W. Sedat, Fast live simultaneous multiwavelength four-dimensional optical microscopy. *Proc. Natl. Acad. Sci.* **107**, 16016–16022 (2010).
92. A. Buades, B. Coll, J. M. Morel, A non-local algorithm for image denoising, in *Proceedings - 2005 IEEE Computer Society Conference on Computer Vision and Pattern Recognition, CVPR 2005* II, (2005), pp. 60–65.
93. V. Duval, J.-F. Aujol, Y. Gousseau, A Bias-variance approach for the nonlocal means. *SIAM J. Imaging Sci.* **4**, 760–788 (2011).
94. I. Frosio, J. Kautz, "On Nearest Neighbors in Non Local Means Denoising. *31st Conference on Neural Information Processing Systems (NIPS 2017)*, arXiv: 1711.07568 [cs.CV] (20 November 2017).
95. O. Lotan, M. Irani, Needle-match: Reliable patch matching under high uncertainty, in *Proceedings of the IEEE Computer Society Conference on Computer Vision and Pattern Recognition 2016-Decem*, (2016), pp. 439–448.
96. M. Maggioni, G. Boracchi, A. Foi, K. Egiazarian, Video denoising, deblocking, and enhancement through separable 4-D nonlocal spatiotemporal transforms. *IEEE Trans. Image Process.* **21**, 3952–3966 (2012).
97. K. Dabov, A. Foi, K. Egiazarian, Video denoising by sparse 3D transform-domain collaborative filtering, in *15th European Signal Processing Conference* (2007), pp. 145–149.
98. S. Zhu, K.-K. Ma, A new diamond search algorithm for fast block-matching motion estimation. *IEEE Trans. Image Process.* **9**, 287–290 (2000).
99. R. Heintzmann, Band limit and appropriate sampling in microscopy. *Cell Biol.* **3**, 29–36 (2006).
100. M. Mäkitalo, A. Foi, Poisson-Gaussian denoising using the exact unbiased inverse of the generalized anscombe transformation, in *ICASSP, IEEE International Conference on Acoustics, Speech and Signal Processing - Proceedings* (2012), pp. 1081–1084.
101. K. Zhang, W. Zuo, Y. Chen, D. Meng, L. Zhang, Beyond a Gaussian denoiser: Residual learning of deep CNN for image denoising. *IEEE Trans. Image Process.* **26**, 3142–3155 (2018).
102. K. He, X. Zhang, S. Ren, J. Sun, Deep residual learning for image recognition, in *Proceedings of the IEEE Conference on Computer Vision and Pattern Recognition* (2016), pp. 770–778.
103. B. Eismann, T. G. Krieger, J. Beneke, R. Bulkescher, L. Adam, H. Erfle, C. Herrmann, R. Eils, C. Conrad, Automated 3D light-sheet screening with high spatiotemporal resolution reveals mitotic phenotypes. *J. Cell Sci.* **133**, jcs245043 (2020).
104. T. Falk, D. Mai, R. Bensch, Ö. Çiçek, A. Abdulkadir, Y. Marrakchi, A. Böhm, J. Deubner, Z. Jäckel, K. Seiwald, A. Dovzhenko, O. Tietz, C. D. Bosco, S. Walsh, D. Saltukoglu, T. L. Tay, M. Prinz, K. Palme, M. Simons, I. Diester, T. Brox, O. Ronneberger, U-Net: Deep learning for cell counting, detection, and morphometry. *Nat. Methods* **16**, 67–70 (2019).
105. M. G. Haberl, C. Churas, L. Tindall, D. Boassa, S. Phan, E. A. Bushong, M. Madany, R. Akay, T. J. Deerinck, S. T. Peltier, M. H. Ellisman, *CDeep3M*—Plug-and-Play cloud-based deep learning for image segmentation. *Nat. Methods* **15**, 677–680 (2018).
106. M. Brady, Computational approaches to image understanding. *ACM Computing Surveys* **14**, 3–71 (1982).
107. T. A. Bubba, G. Kutyniok, M. Lassas, M. Mrz, W. Samek, S. Siltanen, V. Srinivasan, Learning the invisible: A hybrid deep learning-shearlet framework for limited angle computed tomography. *Inverse Probl.* **35**, 064002 (2019).
108. Z. Lyu, C. Zhang, M. Han, DSTnet: A new discrete shearlet transform-based CNN model for image denoising. *Multimed. Syst.* **27**, 1165–1177 (2021).

Acknowledgments: We thank S. Takayama at Georgia Institute of Technology for the useful discussion and for providing us with fluorescently labeled MCF10A mammary 3D organoids. **Funding:** We acknowledge the support of the National Institutes of Health grants R35GM124846 (to S.J.) and R01AA028527 (to C.X.), the National Science Foundation grants BIO2145235 and EFMA1830941 (to S.J.), and Marvin H. and Nita S. Floyd Research Fund (to S.J.). This research project was supported, in part, by the Emory University Integrated Cellular Imaging Microscopy Core and by PHS Grant UL1TR000454 from the Clinical and Translational Science Award Program, National Institutes of Health, and National Center for Advancing Translational Sciences. **Author contributions:** B.M. and S.J. conceived and designed the project. B.M. developed the software. B.M., W.L., and X.H. performed imaging experiments. S.L. prepared the mammalian organoid sample. P.F. prepared the cardiac spheroid sample. J.H. and S.N. prepared the frog embryo sample. B.M. conducted image analysis and generated results. S.N. and C.X. inspected the research results. S.J. supervised the overall project. B.M. and S.J. wrote the manuscript with input from all authors. **Competing interests:** The authors declare that they have no competing interests. **Data and materials availability:** All data needed to evaluate the conclusions in the paper are present in the paper and/or the Supplementary Materials. The code for MIRO is available as Supplementary Software. Additional data are publicly available here: https://doi.org/10.5281/zenodo.8054736. The code has been written in MATLAB (MathWorks) and has been tested with version 2021b. In MATLAB, the software can be run from the command line or using its graphical interface. To install the package, unzip the compressed folder and follow the instructions in the file readme.txt. The most updated version of the software can be found upon publication at: https://github.com/ShuJiaLab/MIRO.

Submitted 13 February 2023
Accepted 31 July 2023
Published 30 August 2023
10.1126/sciadv.adg9245